

Chapter 1

Synthesis of Red and Black Phosphorus Nanomaterials

Yihang Liu,¹ Dingzhou Cui,¹ Mingrui Chen,² Zhen Li,³
and Chongwu Zhou^{1,*}

¹Ming Hsieh Department of Electrical and Computer Engineering,
University of Southern California, Los Angeles, California 90089, United States

²Mork Family Department of Chemical Engineering and Materials Science,
University of Southern California, Los Angeles, California 90089, United States

³Department of Physics, University of Southern California,
Los Angeles, California 90089, United States

*E-mail: chongwuz@usc.edu.

Phosphorus is one of the most common chemical elements found in both person's body and the Earth. Elemental phosphorus exists in several different forms and loosely classified with the colors of white, red, and black. Due to the different crystal structures, the above phosphorus allotropes present very different physical and chemical properties. The blooming of science and engineering in nanoscale enables us to revisit the phosphorus allotropes that has been discovered, and due to the complexity of the phosphorus-phosphorus bond system, many new phosphorus nanomaterials are being created. In this chapter, we will focus on the recent progress of the red and black phosphorus nanomaterial synthesis, and the relevant side topics such as the synthesis of purple and blue phosphorus will also be discussed.

Phosphorus, the element in the 15th group of the periodic table, is the 11th abundant element on the Earth. Since its purification from the organism in 1669, phosphorus has been studied as an important element in plants and animals over 300 years (1). In the era of nanotechnology, phosphorus has been tremendously developed as an inorganic nanomaterial. Phosphorus has the three most common allotropes of white, red, and black phosphorus, whose crystal structures are exhibited in Figure 1 (2). White phosphorus, the first discovered allotrope of phosphorus, consists of fundamental units of tetrahedral P₄ molecules. White phosphorus is soft and waxy due to its molecular structure, and it is very toxic and unstable due to the high angular strain of the P₄ molecule, which promotes the red and black phosphorus nanomaterials into a better position for applications such as energy storage material, field-effect transistor, photodetector, and photocatalyst.

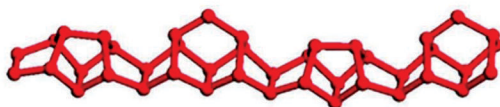
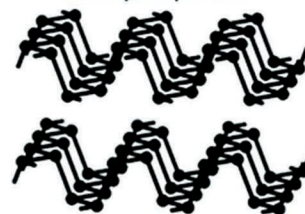
White phosphorus**Red phosphorus****Black phosphorus**

Figure 1. Crystal structures of white phosphorus, red phosphorus, and black phosphorus (2). Reprinted from reference (2). Liu, W.; Zhi, H.; Yu, X. *Recent progress in phosphorus based anode materials for lithium/sodium ion batteries. Energy Storage Mater.* 2019, 16, 290-322, Copyright 2019, with permission from Elsevier.

Synthesis of Red Phosphorus Nanomaterial

Red phosphorus, discovered in 1845, is much more stable than white phosphorus. In industrial, red phosphorus was converted from white phosphorus, which can be produced by reducing the phosphorus in phosphate rocks at high temperature. Usually, the structure of red phosphorus has been usually described to be amorphous and polycrystalline. However, crystalline red phosphorus with different crystal structures has also been reported and studied (3). From white to black, the phosphorus allotropes become more and more stable, and there are several intermediate forms other than red phosphorus between white and black, such as yellow phosphorus (by exposing white phosphorus to light) and violet phosphorus (Hittorf's phosphorus with monoclinic or rhombohedral structure), suggesting the complexity of the P-P system. Red phosphorus has a chain-like structure which can be considered as a bunch of P_4 tetrahedron wherein one P-P bond is broken to form additional bonds with the neighboring tetrahedron, and thus red phosphorus with polymeric structure can be considered as the phase between white phosphorus and violet phosphorus (4). Recently, the study of red phosphorus nanomaterials mainly focused on energy storage applications, where amorphous red phosphorus has been recognized as advantageous because of the relatively small volume change during sodiation and de-sodiation cyclings. While for the photocatalysis study of red phosphorus, crystalline red phosphorus has been reported as an efficient photocatalyst because of the higher charge transfer efficiency (5).

Mechanical Methods

Usually, the synthesis of the red phosphorus nanomaterial starts from bulk phosphorus, and the mechanical milling is the most direct way with relatively good productivity. As a high-capacity anode material for lithium-ion and sodium-ion batteries, red phosphorus suffers from its poor conductivity and huge volume variation during ion intercalation and distraction. In order to address the above issues, several red phosphorus nanomaterials were milled with carbonaceous materials in different dimensions, such as one-dimensional carbon nanotube, two-dimensional graphene, and three-dimensional carbon black. Bulk red phosphorus is broken into nanoparticles and dispersed into the host materials via milling process. Since the carbon black has been widely used as a conductive additive in commercial lithium-ion batteries, there are several reports about the preparation of the phosphorus/carbon nanocomposite through ball-milling commercial red phosphorus with conductive carbonaceous materials, and the electrochemical performance was greatly improved compared to pure phosphorus electrodes (6–9). Dou et al. reported the synthesis of red phosphorus-carbon nanotube composite by grinding commercial red phosphorus with multi-walled carbon

nanotubes, and the scanning electron microscopy (SEM) and transmission electron microscopy (TEM) images of the synthesized nanocomposite are shown in Figure 2 (a) to (c) (10). Wang et al. employed graphene to composite with red phosphorus by the high-energy ball-milling method as the anode material of sodium-ion batteries, demonstrating that the graphene sheets wrap up the red phosphorus nanoparticles during the milling process, which not only enhances the conductivity of the composites, but also accommodates the large volume expansion of red phosphorus during cycling. TEM image with the energy-dispersive X-ray spectroscopy (EDS) elemental mapping profile of carbon and phosphorus are exhibited in Figure 2 (d) to (f) (11).

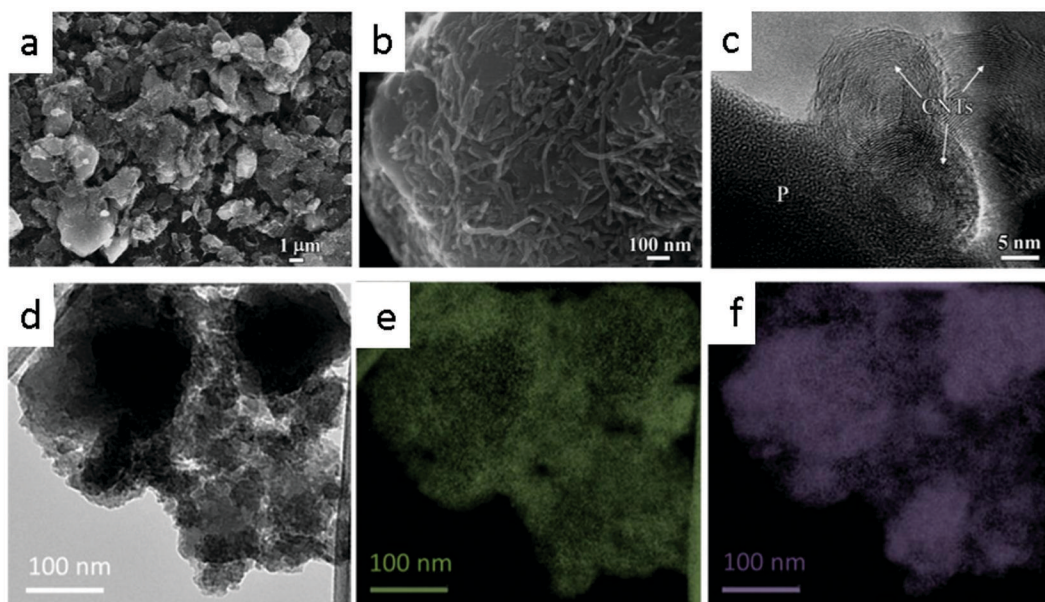


Figure 2. (a, b) EM images of the red phosphorus-carbon nanotube composite under different magnifications. (c) TEM image of the red phosphorus-carbon nanotube composite (10). Reproduced with permission from reference (10). Copyright 2013 American Chemical Society. (d) TEM image of ball-milled red phosphorus-graphene composite with its EDS elemental mapping profiles of carbon and phosphorus presented in (e) and (f) respectively (11). Reproduced with permission from reference (11).

Copyright 2014 American Chemical Society.

Thermal Growth Strategies

Although the mechanical milling method is facile and productive, the size of the produced phosphorus nanomaterial is not uniform because of the rather random process of the milling technique. Compared with milling, thermal vaporization-condensation method has been proved to be more effective in producing uniform red phosphorus nanoparticle and thin film in with the thickness of nanometers, and thus this strategy has been widely adopted to improve the electrochemical performance of phosphorus in battery and photocatalysis applications. When the temperature reaches the sublimation or boiling point of bulk red phosphorus (400-600°C under argon atmosphere or vacuum in sealed glass/quartz ampoule or autoclave), the diffusion of the phosphorus sublimate and vapor is driven by the capillary forces and pressure gradient, and then the phosphorus is absorbed and deposited on the internal and external surface of the substrates and host materials, as illustrated in the schematic in Figure 3 (a). The condensate is subsequently heated to the desired temperature (usually 260-280°C under argon atmosphere or vacuum) for the white-

to-red-phosphorus conversion (12). It has been demonstrated that the vaporization-condensation method is adaptive for various kinds of host materials especially carbonaceous materials including nanotubes, nanofiber, graphene, and three-dimensional porous materials with pore size ranging from nanometers to micrometers. For example, Liu et al. reported the growth of red phosphorus nanodots on reduced graphene oxide as an anode material for sodium-ion batteries, and the flame-retardancy of red phosphorus nanocomposite was also reported in their later studies (13, 14). The size of the red phosphorus nanodots ranges from several to hundreds of nanometers, and the amorphous nature of the nanodots can be observed. The advantages of phosphorus nanodots can be summarized into two aspects: i) minimization of stresses during sodiation/desodiation, which prolongs cycle life, ii) the shortened distance of ion diffusion enabled faster charging/discharging capability. In this work, graphene worked as the electron pathway to enhance the conductivity and ion transport, and the mechanical framework to buffer the volume change of phosphorus active materials. Zhu et al. synthesized red phosphorus-carbon nanotube nanocomposite by heating red phosphorus and single-walled carbon nanotube at 600 °C under vacuum condition. The bulk red phosphorus precursor was vaporized first, and then the vapor diffused into the spaces between and in tangled single-walled carbon nanotubes, providing reliable electronic contact between the phosphorus active material and carbon nanotube bundles, as exhibited in the SEM image in Figure 3 (b) (15). Li et al. reported the vapor-phase strategy with porous carbon nanofibers, demonstrating that deposited phosphorus and the carbon nanofiber can form conductivity networks, and the volume variation can also be effectively buffered due to the porous structure of carbon nanofibers, and the morphology of the synthesized nanocomposite was presented in the SEM image in Figure 3 (c) (16). In this work, the poly-crystalline red phosphorus was loaded into freestanding porous carbon nanofibers with three-dimensional interconnection, and the free-standing and flexible properties of the fabricated electrodes were also demonstrated. On the other hand, three-dimensional carbon materials have been considered as an excellent host scaffold for phosphorus due to their large porosity. The volume variation of phosphorus active material during cycling can be efficiently accommodated by restricting phosphorus within their pores, and high loading mass of the phosphorus can be achieved. On example is the encapsulating phosphorus in the porous carbon matrix. With the vaporization-condensation-conversion strategy, Yu's group confined nanosized amorphous red phosphorus into the space of the highly ordered channels in three-dimensional mesoporous carbon (17). The resulted composite exhibited impressive lithium and sodium-ion battery performance due to the highly uniform channels, large pore volume, and good electronic conductivity of the carbon host. Instead of using mesoporous carbon as the scaffold, the same group also reported a study with the nanoporous metal organic framework (18). With the small nanopores (smaller than 1 nm), lithium and sodium ions in the organic electrolyte can diffuse more efficiently to ensure a better ion transfer kinetics, and the size of the encapsulated red phosphorus particles are further reduced. The TEM image of the synthesized nanocomposite is presented in Figure 3 (d)

Crystalline red phosphorus is another product of the vaporization-condensation synthesis. With iodine as a catalyst, Ruch et al. synthesized crystalline fibrous red phosphorus, whose crystal structure is closely related to the violet phosphorus, as shown in the high-resolution TEM image in Figure 4 (a) (19). With an estimated bandgap of 1.7 eV, the pure crystalline red phosphorus can be considered as a semiconductor and photocatalyst. Previously, amorphous red phosphorus has been incorporated into titanium dioxide to improve the solar spectrum response of TiO₂, where the bandgap of TiO₂ was narrowed by the introduction of red phosphorus (20). Recently, the synthesis of crystalline red phosphorus nanorods on a quartz sheet has been reported by Yu's group, and the SEM image of the nanorods is shown in Figure 4 (b) (21), who followed the recipe presented

by Roth et al. (3) In the first stage of this study, the commercial red phosphorus and water were heated to 200°C in an autoclave to remove surface oxidation, and then the treated red phosphorus was crystallized in a vacuum environment at 450°C for 12 hours. The morphology characterizations suggest that the structure of the product is a layer of nanorods grown on the surface of microparticles. In addition, additives such as bismuth have been used to catalyze the vapor-liquid-solid growth of the crystalline phosphorus nanomaterials, whose SEM image is shown in Figure 4 (c) (22, 23). With the assistance of liquid bismuth nanodroplets, Yu's group also synthesized highly charge polarized single-crystalline phosphorus microbelts (Figure 4 (d)) (24). The temperature was increased to 550°C to enable the vaporization of amorphous red phosphorus and the melting of bismuth, and then the temperature was decreased to 300°C and maintained for 10 hours. Finally, the single crystalline phosphorus microbelts with a surface area of $\sim 1000 \mu\text{m}^2$ and thickness of $\sim 300 \text{ nm}$ are obtained and characterized as Hittorf's phosphorus.

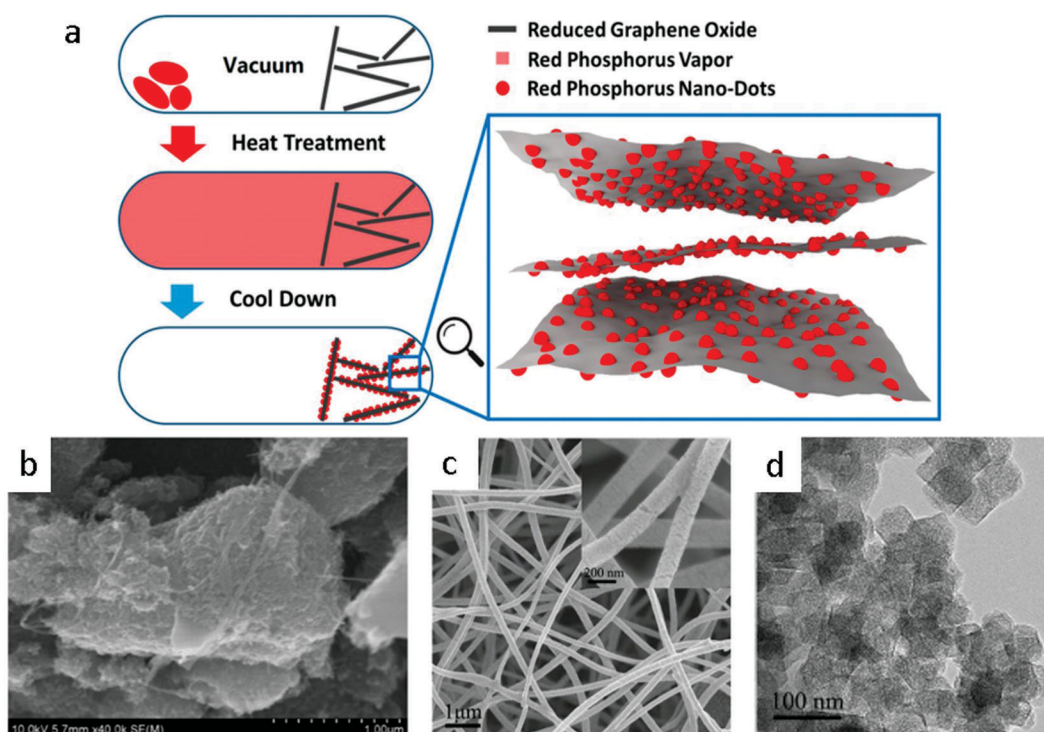


Figure 3. (a) Schematic figure of one example of the vaporization-condensation synthesis method: red phosphorus nanodots on reduced graphene oxide (13). Reproduced with permission from reference (13). Copyright 2017 American Chemical Society. Nanomaterials synthesized by the vaporization-condensation method: (b) SEM image of the red phosphorus-carbon nanotube composite (15). Reproduced with permission from reference (15). Copyright 2014 American Chemical Society. (c) SEM image of the red phosphorus-porous carbon nanofiber composite (16). Reprinted from Li, W.; Yang, Z.; Jiang, Y.; Yu, Z.; Gu, L.; Yu, Y. Crystalline red phosphorus incorporated with porous carbon nanofibers as flexible electrode for high performance lithium-ion batteries. *Carbon* 2014, 78, 455-462, Copyright 2014, with permission from Elsevier. (d) TEM image of the phosphorus-metal organic framework (18). Reproduced with permission from reference (18). Copyright 2017 John Wiley and Sons.

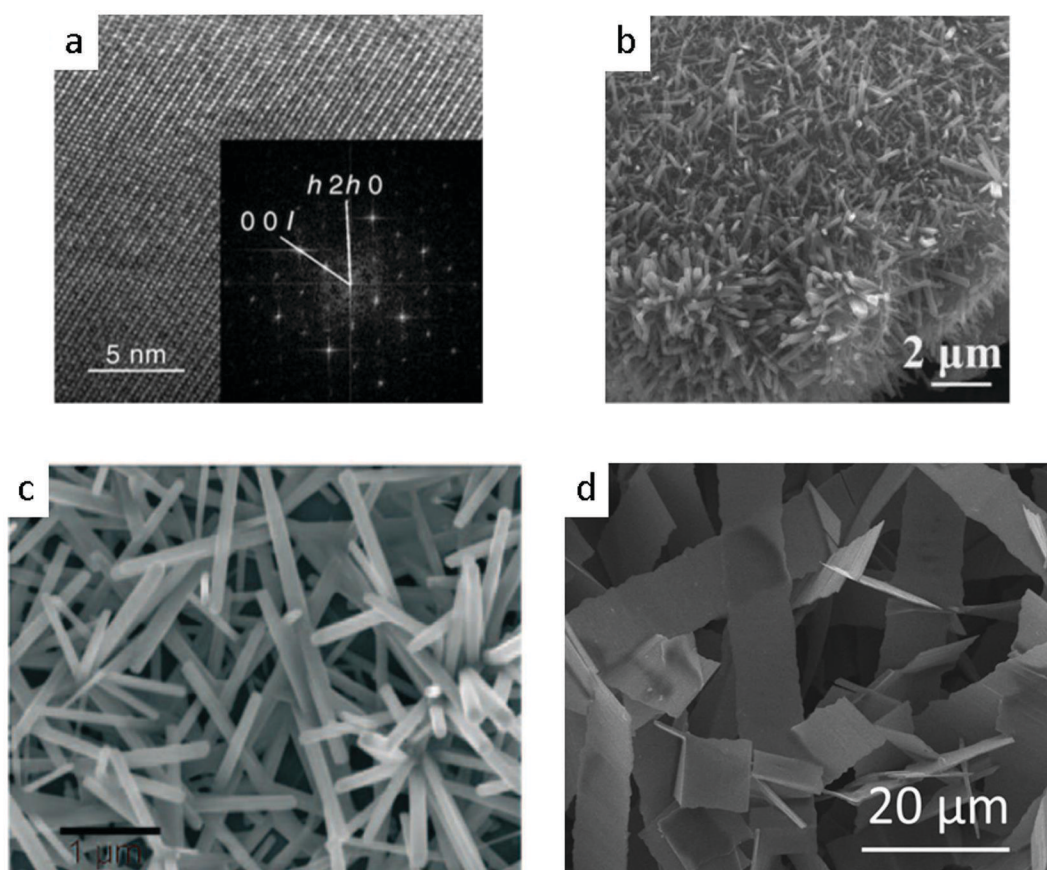


Figure 4. (a) High-resolution TEM image and selected area diffraction pattern of the fibrous red phosphorus synthesized with iodine as a catalyst (19). Reproduced with permission from reference (19). Copyright 2005 John Wiley and Sons. (b) Crystalline red phosphorus synthesized by heating amorphous phosphorus under vacuum (21). Reprinted from Wang, F.; Ng, W. K. H.; Jimmy, C. Y.; Zhu, H.; Li, C.; Zhang, L.; Liu, Z.; Li, Q. Red phosphorus: an elemental photocatalyst for hydrogen formation from water. *Appl. Catal., B* 2012, 111, 409-414, Copyright 2012, with permission from Elsevier. (c) SEM image of the crystalline red phosphorus nanorods synthesized on the bismuth-doped silicon wafer (23). Reproduced with permission from reference (23). Copyright 2009 John Wiley and Sons. (d) SEM image of the Hittorf's phosphorus microbelt synthesized with the assistance of bismuth nanodroplet (24). Reprinted from Liu, Y.; Hu, Z.; Jimmy, C. Y. Liquid bismuth initiated growth of phosphorus microbelts with efficient charge polarization for photocatalysis. *Appl. Catal., B* 2019, 247, 100-106, Copyright 2019, with permission from Elsevier.

Compare to the top-down mechanical milling technique, the thermal growth strategy is a bottom-up synthesis method which can realize the uniform growth of amorphous or crystalline red phosphorus nanomaterial, on both outer and inner surface of the scaffold without damaging the structure and morphology of the scaffold material. However, considering the rather complicated synthesis process, the production rate of the thermal growth method is usually low, and safety considerations are also brought on to the table due to the existing of white phosphorus as the intermediate product.

Other Methods

Other than the above synthesis methods, the solution-phase approach is another competitive candidate for the large-scale production of red phosphorus nanomaterials. Recently, Liu et al. demonstrated a solution route to synthesize iodine-doped red phosphorus nanoparticles by reacting PI_3 with ethylene glycol in the presence of cetyltrimethylammonium bromide (CTAB). The synthesized red phosphorus nanoparticles are uniform in size, as shown in the SEM image in Figure 5 (a) (25). Liu, et al, reported a redox reaction to synthesize porous red phosphorus nanoparticles on graphene sheets. The sample was prepared by adding hydrazine hydrate ($\text{N}_2\text{H}_4\cdot\text{H}_2\text{O}$) into a mixture of PI_3 , iodobenzene, graphene oxide, CTAB, and ethylene glycol, and the TEM image of the particles is shown in Figure 5 (b) (26). Furthermore, via the solution process, red phosphorus with specifically designed morphologies can be synthesized. Zhou, et al, reported the wet-chemical synthesis of amorphous hollow red-phosphorus nanospheres, whose TEM image is exhibited in Figure 5 (c) (27). A solution of PCl_5 and Na_3N in toluene was used as the precursor, and then a solvothermal process was performed to produce hollow red-phosphorus nanospheres through a gas-bubble-directed formation mechanism. The porous and hollow structures boosted the electrochemical performance of phosphorus nanomaterials in the sodium-ion battery system. The solution-phase strategy can avoid the high portion of carbon or host material in the active red phosphorus nanomaterials, and the size and morphology of the product are uniform and controllable. Although it is difficult to remove the introduced impurities, considering that this solution-phase method for nanomaterial synthesis has been well-studied in the last few decades, it is reasonable to believe that this route could lead to the exquisite synthesis of various red phosphorus nanomaterials in the future.



Figure 5. (a) SEM image of the iodine doped red phosphorus nanosphere (25). Reproduced with permission from reference (25). Copyright 2017 American Chemical Society. (b) TEM image of the porous red phosphorus nanoparticles on graphene (26). Reproduced with permission from reference (26). Copyright 2018 American Chemical Society. (c) TEM image of the red phosphorus hollow sphere synthesized through the solution route (27). Reproduced with permission from reference (27). Reproduced with permission from reference (27). Copyright 2017 John Wiley and Sons.

In addition to the synthesis routes mentioned above, several methods have been combined together to complete more complicated synthesis processes. For example, the sonication is another mechanical route to break red phosphorus bulk material into nanoparticles to obtain a suspension, and it has been widely used as a pretreatment in the synthesis flow. Gao et al. obtained a red phosphorus/graphene suspension through sonication, and then embedding red phosphorus nanoparticle into graphene aerogel by the co-freeze-drying and vapor re-distribution methods (28).

In another example, commercial red phosphorus was first ball-milled, and the resulted red phosphorus nanoparticles were selected by the buoyancy force of water, and finally, sonication and freeze-drying techniques were employed to the mixture of red phosphorus suspension and graphene oxide solution to obtain the phosphorus-graphene products (29). In addition, using the carbothermic reduction method with the assistance of sunlight, a three-dimensional-structured phosphorus/carbon composite was synthesized starting from P_4O_{10} , and the resulted ultrafine red phosphorus particles with a diameter of around 10 nm were linked onto three-dimensional carbon framework via chemical bonds (30). The carbon framework not only enhances the electrical conductivity, but also provide enough buffer space to accommodate the large volume expansion of phosphorus during sodiation and de-sodiation processes.

Synthesis of Black Phosphorus Nanomaterial

Black phosphorus is the phosphorus allotrope with the highest thermodynamic stability. It is a layered material resembling graphite in texture, and with a puckered structure in which each phosphorus atom is covalently bonded to its three nearest neighbors. It has tremendously different properties from other allotropes as it is black, flaky, and built up of indented sheet-like layers of linked atoms. The layer distance of black phosphorus is around 5.2 Å. The unique crystal structure of black phosphorus ensures a high electronic conductivity (~ 300 S/m), and the bandgap of 0.3 to 2 eV was observed from monolayer to bulk material (31). Due to its unique structure and properties, the field-effect transistor (FET), photodetector, catalyst, and battery performances of black phosphorus have been intensively studied recently.

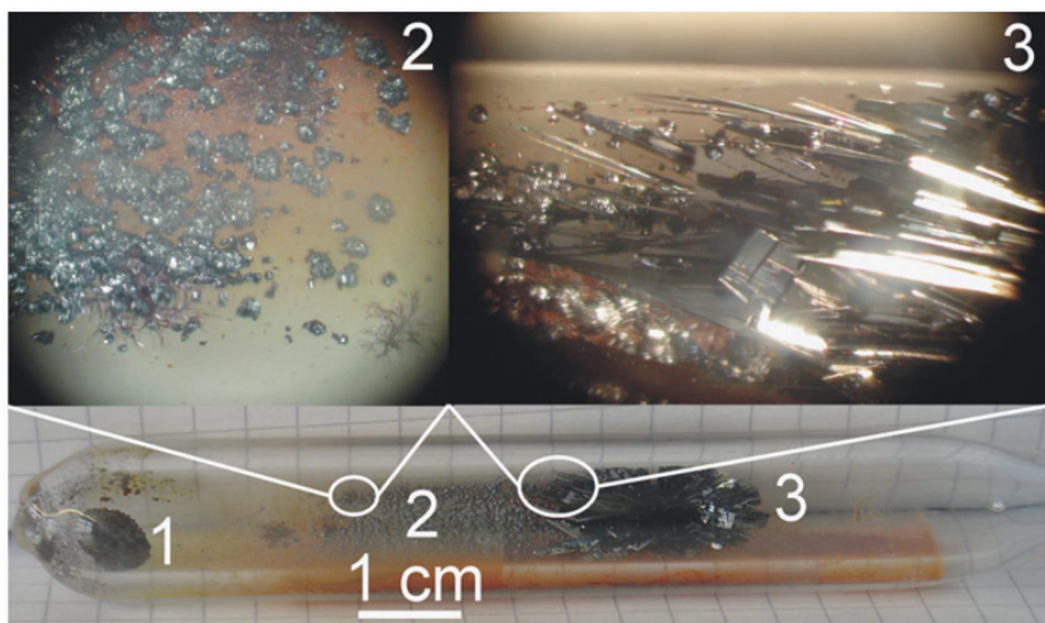


Figure 6. Optical image of the low-pressure transport route synthesized large black phosphorus single crystals in a silica ampoule, where areas marked with 1, 2 and 3 represent the bulk precursor residue, violet phosphorus and the black phosphorus as the main product, respectively (38). Reprinted from Nilges, T.; Kersting, M.; Pfeifer, T. A fast low-pressure transport route to large black phosphorus single crystals. *J. Solid State Chem.* 2008, 181 (8), 1707-1711, Copyright 2008, with permission from Elsevier.

The study of black phosphorus synthesis has never been stopped, since its discovery in 1914 by converting white phosphorus at a moderate temperature under high pressure (32–36). In the past decades, several synthesis works of the high-quality and large-size black phosphorus crystal have been reported, one of the resulted product can be found in the optical photos in Figure 6 (37–39). In contrast to the traditional conversation from red/white phosphorus to black phosphorus under high pressure, the vapor growth of black phosphorus is usually carried with the low-pressure transport reaction, where red phosphorus and catalysts are sealed inside a quartz ampoule under vacuum, and the ampoule is heated above the boiling point of red phosphorus to generate P_4 vapor, which will finally deposit onto the surface of catalysts and form black phosphorus crystals.

Exfoliation

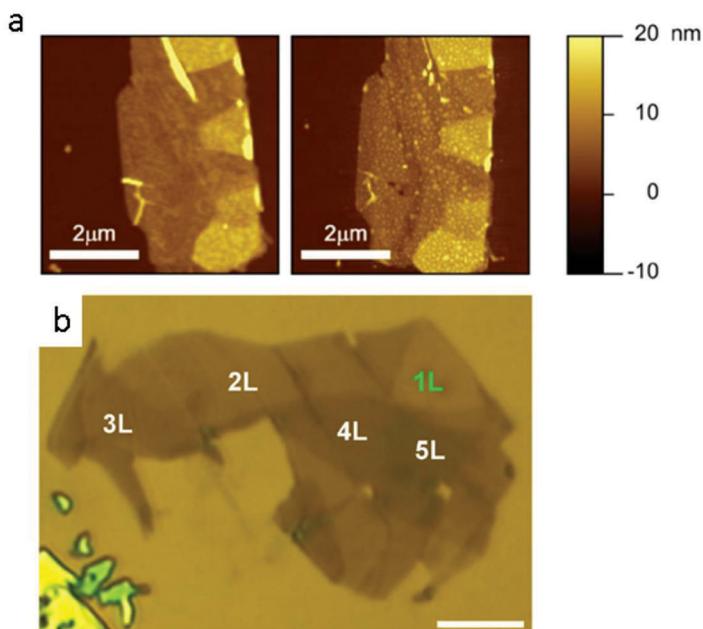


Figure 7. (a) AFM images of a piece of black phosphorus flake obtained immediately after cleaving (left) and after exposure to air for 3 days (right) (40). Reprinted by permission from Springer Nature Customer Service Centre GmbH: Springer Nature, *Nature Nanotechnology*, Li, L.; Yu, Y.; Ye, G. J.; Ge, Q.; Ou, X.; Wu, H.; Feng, D.; Chen, X. H.; Zhang, Y. Black phosphorus field-effect transistors. *Nat. Nanotechnol.* 2014, 9 (5), 372. Copyright 2014.. (b) Optical image of multilayered phosphorene after Ar^+ plasma thinning. Scale bar is $5 \mu m$ (43). Reprinted by permission from Springer Nature Customer Service Centre GmbH: Springer Nature, *Nano Research*, Lu, W.; Nan, H.; Hong, J.; Chen, Y.; Zhu, C.; Liang, Z.; Ma, X.; Ni, Z.; Jin, C.; Zhang, Z. Plasma-assisted fabrication of monolayer phosphorene and its Raman characterization. *Nano Res.* 2014, 7 (6), 853-859. Copyright 2014.

Same as the other two-dimensional materials such as transition metal dichalcogenide (TMDC) and boron nitride, monolayer or few-layer black phosphorus (phosphorene) can be prepared by mechanical exfoliation, borrowing the idea from the discovery of graphene. This process involves using adhesive tape to cleave bulk layered materials into monolayer or few-layer nanoflakes. Liu et al. and Li et al. reported the Scotch-tape-based microcleavage of few-layer black phosphorus for FET study (40, 41). One example of the tape-exfoliated black phosphorus can be found in the atomic force microscopy (AFM) image in Figure 7 (a), and then dots were observed on the flake due to

the oxidization in air. The as-prepared phosphorene was used to fabricate FETs and exhibited high mobilities up to $1000 \text{ cm}^2 \text{ V}^{-1} \text{ s}^{-1}$ at room temperature and on/off ratios in the scale of 10^4 .

Although the mechanical tape exfoliation is a facial and effective method to prepare black phosphorus nanomaterials for research proposes, its low yield and potential contamination make this method not suitable for the large-scale production. Thus, several other exfoliation methods have been developed to address the above issue. Castellanos-Gomez et al. developed a modified mechanical exfoliation method, in which an intermediate viscoelastic surface was employed to exfoliate the flakes. Briefly, a piece of bulk black phosphorus was cleaved repeatedly by blue Nitto tape for several times. The tape with few-layer black phosphorus flakes is then gently pressed onto the surface of a polydimethylsiloxane (PDMS) substrate to peel off rapidly. This method substantially increased the yield and reduced the contamination of the fabricated nanoflakes (42). Lu et al. successfully demonstrated an approach to fabricate monolayer phosphorene on the substrate by combining mechanical cleavage and plasma treatment, where the few-layer black phosphorus is firstly prepared by mechanical exfoliation on the substrate, and then argon plasma was employed to thin down the few-layer nanoflake to monolayer phosphorene, as the optical image shown in Figure 7 (b) (43).

Other than the tape exfoliation, liquid exfoliation is a low-cost and facial method to obtain monolayer and few-layer black phosphorus nanoflakes with reasonably good production yield, and it is potentially suitable to assemble the large-area thin film on substrates towards the wafer-scale device fabrication. The liquid exfoliation process usually starts with a piece of black phosphorus crystal in a solvent. In order to generate nanosheets with large surface area, the ion exchange and intercalation can be used to weaken the van der Waals interaction between layers. After that, the ultrasonic power could be introduced to accelerate the exfoliation process to obtain the black phosphorus nanosheets suspension. Brent et al. have demonstrated the liquid exfoliation of black phosphorus in N-methyl-2pyrrolidone (NMP) with bath ultrasonication. The obtained turbid dispersions were further purified by centrifugation to remove large solids, resulting in the monolayer and few-layer black phosphorus suspension (44). Yasaei et al. prepared thin black phosphorus nanoflakes using a similar technique (45). They investigated the effects of different solvents and presented that aprotic and polar solvents were preferred for the preparation of a uniform and stable suspension containing atomically thin black phosphorus nanoflakes, for instances, dimethylformamide (DMF) and dimethyl sulfoxide (DMSO). Utilizing the liquid exfoliation of black phosphorus and the self-assembly with graphene, Sun et al. prepared a sandwich structured graphene–black phosphorus nanocomposite, which showed impressive capacity retention and rate capabilities in sodium-ion batteries. The graphene sheets provide an elastic buffer accommodating the expansion of exfoliated black phosphorus nanosheets along planar y and z axes during the sodiation process (46).

Previous studies have proved the hygroscopic nature of black phosphorus, which is unstable in the ambient condition with the presence of water and oxygen. As a result, the liquid exfoliation process needs to be done in anhydrous and oxygen-free organic solvents to minimize the degradation of black phosphorus. Kang et al. conducted the liquid exfoliation in a sealed-tip ultrasonication system with anhydrous organic solvents. Such setup efficiently prevented black phosphorus from degradation via solvated oxygen or water, and the schematic diagram of the experimental setup and the analysis of the suspension with different centrifugation conditions are exhibited in Figure 8 (a) to (d) (47). Hanlon et al. demonstrated that stable and large-quantity production of black phosphorus nanosheet suspensions can be achieved with N-cyclohexyl-2-pyrrolidone (CHP) as the solvent under ambient conditions. A plausible explanation is that the solvation shell can protect black phosphorus nanosheets from side reactions (48). Distinct from previous work, Chen et al. (49)

presented that a clean exfoliation process can be done in water by utilizing the hydrophilic nature of black phosphorus, asserting that it is difficult to remove the residue of the high-boiling-point solvents such as N-Methyl-2-pyrrolidone (NMP) and DMSO. They also estimated the stability of their black phosphorus water suspension and found that only 10 wt% of the black phosphorus nanosheets was dissolved after one week, and there is still 60 wt% of the nanosheets left after eight weeks. The exfoliated black phosphorus suspension was combined with graphene to fabricate flexible electrodes for lithium-ion batteries.

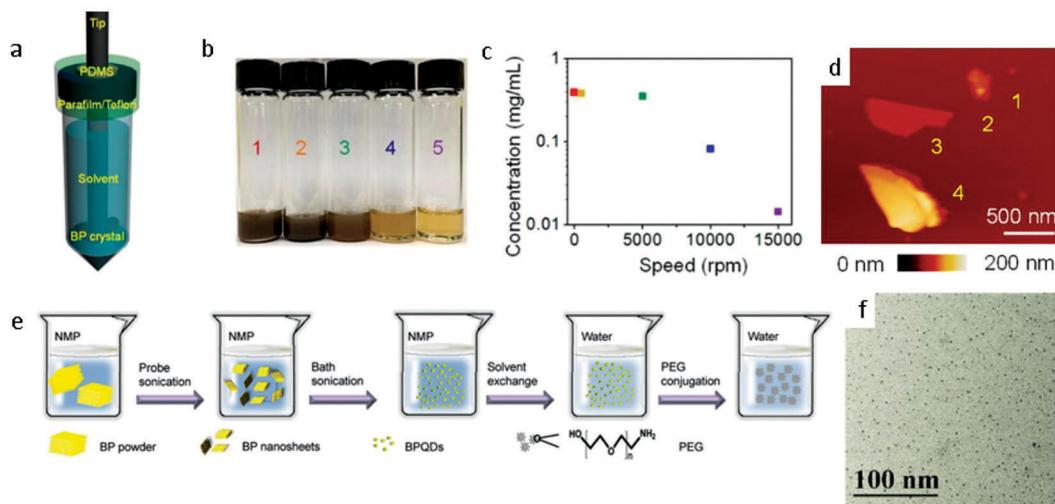


Figure 8. (a) Schematic diagram of the solvent exfoliation of black phosphorus in various solvents via tip ultrasonication (47). Reproduced with permission from reference (47). Copyright 2015 American Chemical Society. (b) Optical photograph of solvent-exfoliated black phosphorus dispersions in NMP solvent with various centrifugation conditions (1: as-prepared, 2:500 rpm, 3:5000 rpm, 4:10000 rpm, and 5:15000 rpm) (47). Reproduced with permission from reference (47). Copyright 2015 American Chemical Society. (c) Concentration of black phosphorus dispersions from part (b) (47). Reproduced with permission from reference (47). Copyright 2015 American Chemical Society. (d) AFM height profile of black phosphorus nanosheets in (b). Black phosphorus solution was deposited onto a 300 Si substrate with 300nm SiO₂ for measurement. The heights are 1:16, 2:40, 3:29, and 4:128 nm (47). Reproduced with permission from reference (47). Copyright 2015 American Chemical Society. (e) and (f) Preparation diagram and TEM characterization of liquid exfoliated black phosphorus quantum dots (50). Reproduced with permission from reference (50). Copyright 2015 John Wiley and Sons.

In contrast to large nanosheets obtained by liquid exfoliation, Sun et al. exfoliated black phosphorus quantum dots combining probe sonication and bath sonication, and the process is illustrated in Figure 8 (e) (50). The as-prepared black phosphorus quantum dots have a diameter and thickness of approximately 2.6 nm and 1.5 nm, respectively, as shown in TEM image in Figure 8 (f), and exhibited excellent near-infrared photothermal performance. This process involves ultrasound probe sonication followed by ice-bath sonication of bulk black phosphorus powder in NMP. The ultrasmall black phosphorus quantum dots obtained by centrifugation were dispersed in water, and polyethylene glycol (PEG) was conjugated to enhance their stability in physiological medium. On the other hand, Zhang et al. combined grinding and liquid exfoliation processes and obtained black phosphorus quantum dots in a similar dimension (51).

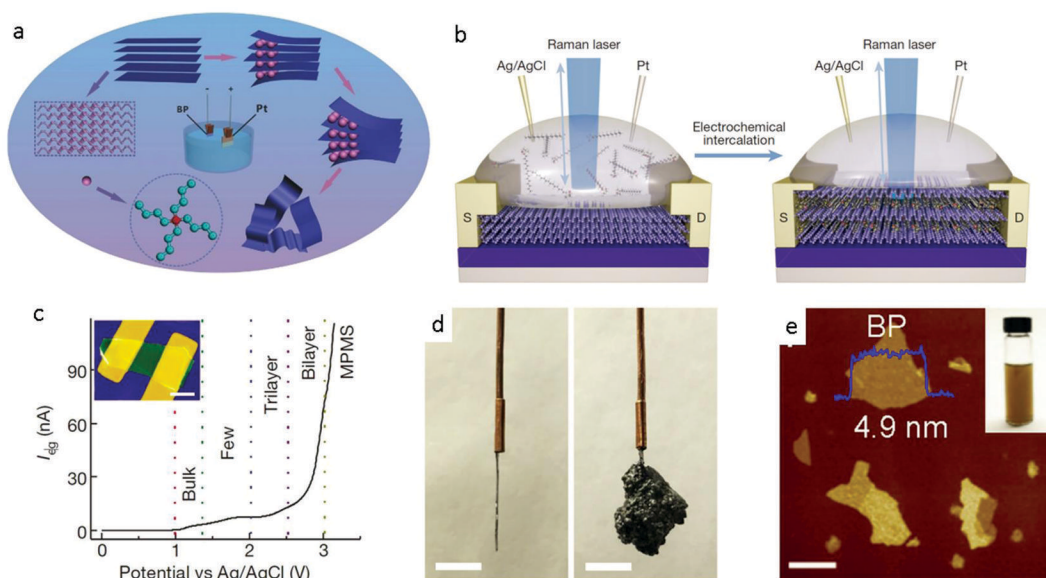


Figure 9. (a) Schematic diagram of the electrochemical exfoliation process of phosphorene using tetrabutylammonium hexafluorophosphate (TBAP) and DMF as the electrolyte (54). Reproduced with permission from reference (54). Copyright 2017 John Wiley and Sons (b) Schematic of the in-situ Raman measurement setup to monitor electrochemical intercalation process of black phosphorus, (left: before intercalation, right: after intercalation) where the cetyl-trimethylammonium bromide (CTAB) and NMP were used as the electrolyte (56). (c) Electrochemical gate current as a function of the applied electrochemical voltage potential, where the inset is the false-color scanning electron microscope (SEM) image of the intercalated black phosphorus transistors with the scale bar of 5 μm (56). Reprinted by permission from Springer Nature Customer Service Centre GmbH: Springer Nature, Nature, Wang, C.; He, Q.; Halim, U.; Liu, Y.; Zhu, E.; Lin, Z.; Xiao, H.; Duan, X.; Feng, Z.; Cheng, R.; Weiss, N.; Ye, G.; Huang, Y. C.; Wu, H.; Cheng, H. C.; Shakir, I.; Liao, L.; Chen, X.; Goddard, W.; Huang, Y.; Duan, X. Monolayer atomic crystal molecular superlattices. *Nature* 2018, 555, 231-236. Copyright 2018. (d) Optical images of a piece of MoS₂ crystal before (left) and after (right) THAB intercalation. The scale bars of 5 mm (57). Reprinted by permission from Springer Nature Customer Service Centre GmbH: Springer Nature, Nature, Lin, Z.; Liu, Y.; Halim, U.; Ding, M.; Liu, Y.; Wang, Y.; Jia, C.; Chen, P.; Duan, X.; Wang, C. Solution-processable 2D semiconductors for high-performance large-area electronics. *Nature* 2018, 562 (7726), 254. Copyright 2018. (e) AFM image of the exfoliated black phosphorus with the quaternary ammonium intercalation (57). Reprinted by permission from Springer Nature Customer Service Centre GmbH: Springer Nature, Nature, Lin, Z.; Liu, Y.; Halim, U.; Ding, M.; Liu, Y.; Wang, Y.; Jia, C.; Chen, P.; Duan, X.; Wang, C. Solution-processable 2D semiconductors for high-performance large-area electronics. *Nature* 2018, 562 (7726), 254. Copyright 2018.

Liquid phase exfoliation of few-layer phosphorene has been extensively explored in recent years. Nevertheless, there are several disadvantages of liquid-phase exfoliation (i) ultralong sonication time makes the process not efficient and may also lead to (ii) small flake size, (iii) many defects and (iv) uncontrolled thickness. The development of more efficient methods is need. In the process of electrochemical exfoliation, an applied voltage drives ions from the electrolyte to intercalate into bulk layered materials to exfoliate individual layer. In contrast to the liquid-phase and mechanical exfoliation, electrochemical exfoliation is more efficient, and the layer number is tunable. Erande et al. employed electrochemical exfoliation to prepare black phosphorus nanosheet for field emitters,

humidity sensing, and photodetection, which shows excellent performance. To prepare black phosphorus nanosheet, bulk black phosphorus and platinum wire were used as two electrodes, the Na_2SO_4 solution was used as the electrolyte. The voltage difference between the two electrodes was 7 V and the corresponding current was ~ 1 mA (52, 53). Afterward, Huang et al. introduced an electrochemical cationic intercalation method to prepare large-area, layer number controllable few-layer black phosphorus, whose schematic is shown in Fig 9 (a) (54). In their method, bulk black phosphorus was used as the cathode, and the electrolyte was prepared by dissolving tetrabutylammonium perchlorate (TBAP) in dimethylformamide (DMF). The layer number can be controlled by the intercalation rate of tetraalkylammonium cations. Phosphorene with various layers (from 2 to 11) were obtained with different applied voltage potentials. Li et al. reported an ultrafast electrochemical exfoliation method for bulk black phosphorus, which takes only minutes to expand the bulk materials (55). The electrolyte was designed to be tetraalkylammonium (TAA) dissolved in DMSO. A cathodic voltage lower than -5 V can lead to such ultrafast exfoliation process of bulk black phosphorus. In this electrolyte, nonoxidative few-layer black phosphorus nanoflakes can be exfoliated with high-yield (higher than 80%), high crystallinity under ambient conditions. Duan's group reported an electrochemical strategy for black phosphorus exfoliation using cetyltrimethylammonium bromide (CTAB) and NMP as the electrolyte, as illustrated in Figure 9 (b). With Ag/AgCl as the reference electrode, monolayer atomic crystal molecular superlattices can be formed when the voltage increased to 3 V, as presented in Figure 9 (c) (56). Afterward, the same group reported a general method to prepare uniform, solution-processable, and phase-pure semiconducting nanoflakes (57). The process involves electrochemical intercalation of quaternary ammonium molecules into the bulk counterparts of various two-dimensional materials, and then a mild sonication was introduced to fully exfoliate the expanded bulk materials into nanoflakes. Quaternary ammonium bromide dissolved in acetonitrile was used as the electrolyte. The bulk materials to be exfoliated served as the cathode and the voltage bias applied between electrodes was set to be 5-10 V during a 1-hour intercalation process. The optical photos of the MoS_2 bulk crystal before and after the electrochemical intercalation are presented in Figure 9 (d), and the image of the exfoliated black phosphorus with this method is exhibited in Figure 9 (e), with the optical photo of the suspension inserted. In contrast to the electrochemistry-assisted exfoliation, Bat-Erdene et al. reported a microwave-assisted liquid-phase exfoliation method to produce crystalline black phosphorus nanoflakes with low oxidation degree, where the microwave can weaken the van der Waals interaction between black phosphorus layers. Moreover, this method is free of surfactant or sonication and can be completed in a short time (58).

Bottom-Up Growth Strategies

Compare to the top-down exfoliation, deposition techniques such as chemical vapor deposition (CVD), physical vapor deposition (PVD), and molecule beam epitaxial (MBE) are known as the bottom-up method. These methods enable directly synthesis of black phosphorus thin film on various substrates, making it more convenient for further electronic device studies.

CVD is a facial, effective and versatile tool for the synthesis of materials on substrates, and it has been well studied on various two-dimensional materials such as TMDCs and graphene. Highly crystalline, large grain size and layer number controllable two-dimensional materials can be easily grown by CVD. So far, CVD synthesis of black phosphorus has not been studied too much. Smith et al. presented an *in-situ* chemical vapor deposition approach for the growth of large-area two-dimensional black phosphorus, whose experimental setup is illustrated in Figure 10 (a) (59). The

average areas are larger than $3 \mu\text{m}^2$ with the thickness around four layers. As the thickness increases, the average surface area of the deposited black phosphorus film can be larger than $100 \mu\text{m}^2$. In their method, red phosphorus thin films were firstly deposited on the silicon substrate by heating red phosphorus powder or bulk black phosphorus to 600°C under vacuum with a tube furnace. Then, red phosphorus on the silicon substrate was placed into a pressure vessel reactor filled by argon gas. With Sn and SnI_4 as mineralizing agents, the vessel was subsequently put inside the tube furnace before rising temperature to 950°C . It was then chilling at a rate of 50°C every 30 minutes once reached 950°C . Finally, when reached 700°C and 600°C , the temperature was held for 1 hour respectively until the furnace can be turned off completely. Yang et al. reported the amorphous black phosphorus deposited by pulsed laser deposition (PLD) using bulk black phosphorus crystal as the target, the cross-sectional TEM image of the film is exhibited in Figure 10 (b) (60). In contrast to the synthesis of bulk black phosphorus which requires extreme conditions of high pressure and high temperature, such large-scale amorphous black phosphorus ultrathin films with tunable direct bandgap can be synthesized under a mild condition of temperature as low as 150°C by conventional PLD. In this study, FETs based on amorphous black phosphorus were demonstrated. They also presented that 2 nm thick amorphous black phosphorus channel gives relatively high mobility of up to $14 \text{ cm}^2 \text{ V}^{-1} \text{ s}^{-1}$ and moderate on/off ratio of 10^2 for the fabricated FETs with PLD method. Xu et al. directly grew few-layer black phosphorus quantum dots on silicon substrates using MBE. AFM characterization results of the sample are presented in Figure 10 (c) and (d) (61). Fully deoxidized Si(111) or native oxide covered Si(100) wafer were employed as substrates for growth of quantum dots. Then, white phosphorus sealed in a cracker cell was evaporated at 900°C for a 20min deposition process. An average radius of $27.5 \pm 5 \text{ nm}$ and a height of $3.1 \pm 0.6 \text{ nm}$ were observed by AFM at surface steps on fully deoxidized Si(111) substrates. Jiang et al. developed a facile strategy for preparation of black phosphorus thin-film on Ti foil through a thermal-vaporization transformation method without using high pressure (62). The pretreated red phosphorus powder was first annealed at 450°C to be vaporized and deposited on Ti foil. Then, subsequent thermal treatment at 650°C transforms red phosphorus into black phosphorus. The as-prepared black phosphorus shows advanced electrocatalytic activity for the oxygen evolution reaction (OER).

The bottom-up growth method cannot only produce black phosphorus thin film, but also the blue phosphorus, which is a new phase of phosphorus which has been discovered and studied recently. Similar to black phosphorus, the blue phosphorus has been predicted with the layered structure and good thermal stability, and the crystal structure of black and blue phosphorus can be found in Figure 11 (a) and (b) (63). Zhang et al. reported a method for the growth of mono-layer blue phosphorus on Au(111) substrate by molecular beam epitaxial (MBE) (64). Phosphorus was firstly deposited by evaporation of bulk black phosphorus at 260°C from a crucible. The grown monolayer blue phosphorus can be confirmed by high-resolution scanning tunneling microscope (STM). Figure 11 (c) shows the highly ordered superstructure of monolayer blue phosphorus, where each dark center is surrounded by six triangles. The unit cell marked with yellow quadrilateral in Figure 11 (d) was measured as $a = b = 14.7 \text{ \AA}$. After this work, Xu et al. reported similar MBE growth of monolayer blue phosphorus using InP as the precursor (65). They have proposed a growth mechanism involves a dewetting process for the seed nucleation and following growth of single-layer blue-phosphorus-like islands. Besides the MBE growth, they also found a one-dimensional chain structure formed when the blue phosphorus coverage on the substrate was low. In a large range of coverage, a hybrid surface can be observed, which locally high-coverage blue phosphorus islands are surrounded by locally low-coverage one-dimensional chain-like blue phosphorus. Such phase-separated surface configuration

is more preferred than the P-trimer or homogeneous $(\sqrt{3} \times \sqrt{3})R30^\circ$ covered surfaces. This phenomenon can be elucidated from the energy-minimization point of view, which has been proved in the growth of various materials. It is worth mentioning that the interaction between substrate and blue phosphorus is important to the growth process. To form a free-standing mono-layer blue phosphorus, a well-designed substrate that can minimize this interaction is highly desired. Gu et al. demonstrated an approach to prepare quasi-free-standing blue phosphorus monolayer. A tellurium-functionalized gold substrate (Te/Au(111)) was employed in this method (66). The Au(111) substrate was first kept at 300° C, while the Te layer was deposited on it through evaporation of Te source at 200 °C. Bulk black phosphorus was then evaporated at 290°C for the deposition of monolayer blue phosphorus onto the existing Te/Au(111) which was kept at 250°C. XPS revealed that peak shapes and peak positions of both Te 3d and Au 4f remain unchanged before and after the deposition of blue phosphorus, which is the evidence of weak interaction between Te/Au(111) and blue phosphorus.

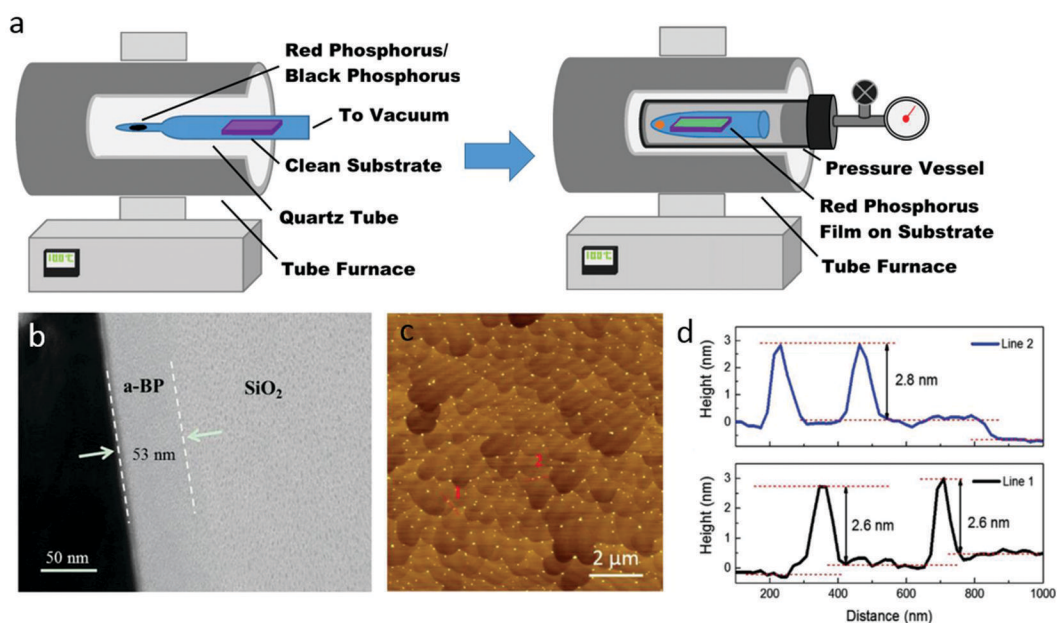


Figure 10. (a) Schematic for CVD growth of black phosphorus (59). Republished with permission of IOP Publishing, from Smith, J. B.; Hagaman, D.; Ji, H.-F. Growth of 2D black phosphorus film from chemical vapor deposition. *Nanotechnology* 2016, 27 (21), 215602. (b) Cross-sectional TEM images of amorphous black phosphorus thin films synthesized by PLD method (60). Reproduced with permission from reference (60). Copyright 2015 John Wiley and Sons. (c) AFM morphology of the black phosphorus quantum dots on silicon substrate synthesized by MBE method (61). Reproduced with permission from reference (61). Copyright 2018 John Wiley and Sons. (d) Height profiles along line 1 and 2, respectively (61). Reproduced with permission from reference (61). Copyright 2018 John Wiley and Sons.

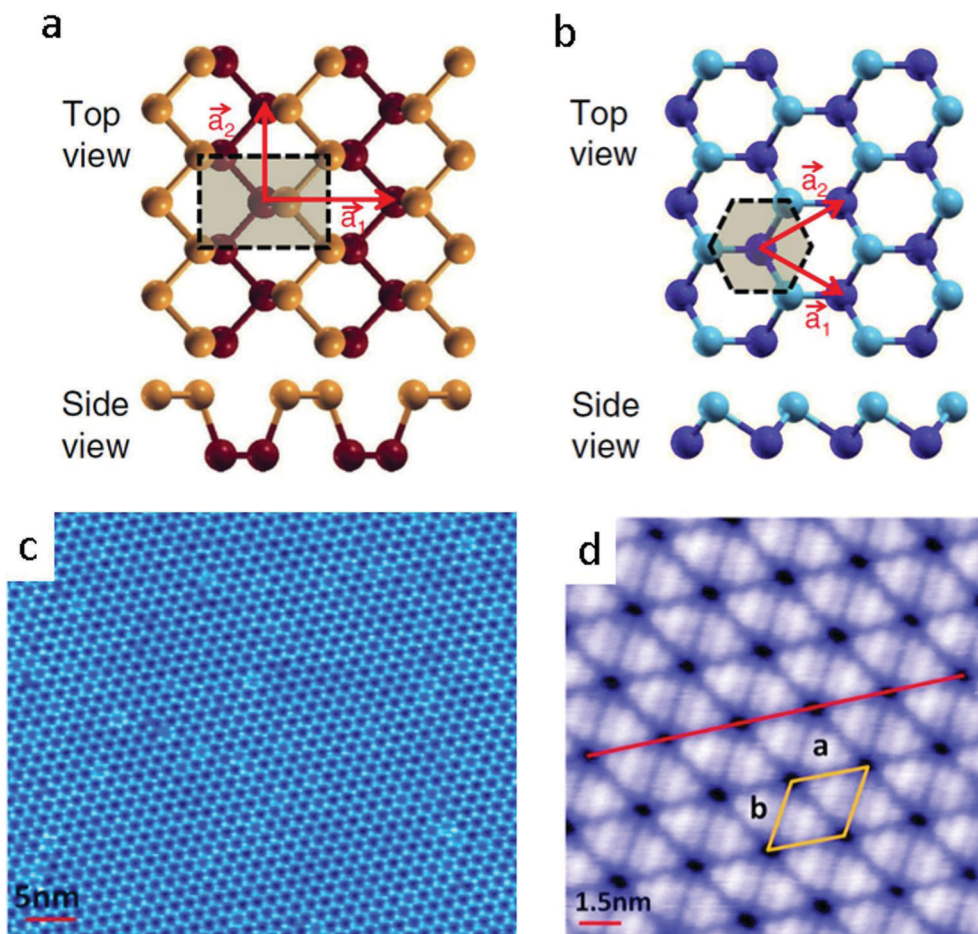


Figure 11. (a, b) Crystal structure of black phosphorus and blue phosphorus (63). Reprinted figure with permission from reference (63). Zhu, Z.; Tománek, D. Semiconducting layered blue phosphorus: a computational study. *Phys. Rev. Lett.* 2014, 112 (17), 176802. Copyright 2014 by the American Physical Society (c) Close-up STM images and (d) High-resolution STM image (64). The unit cell of the phosphorus is measured as $a = b = 14.7 \text{ \AA}$. Reproduced with permission from reference (64). Copyright 2016 American Chemical Society.

High-Pressure Conversion

Since the ball-milling and sonication techniques can introduce high-pressure locally, a few works also reported the synthesis of black phosphorus through this technique for energy storage applications. Park et al. added red phosphorus and carbon into a hardened steel vial, and used high-energy ball-milling technique under argon atmosphere for 54 hours to synthesize black phosphorus/carbon nanocomposite, whose TEM and selected area diffraction pattern are exhibited in Figure 12 (a) (6). Starting from the red phosphorus water suspension, Aldave et al. reported the work using both tip and bath sonicator to synthesize black phosphorus, which was separated from red phosphorus through vacuum filtration finally (67).

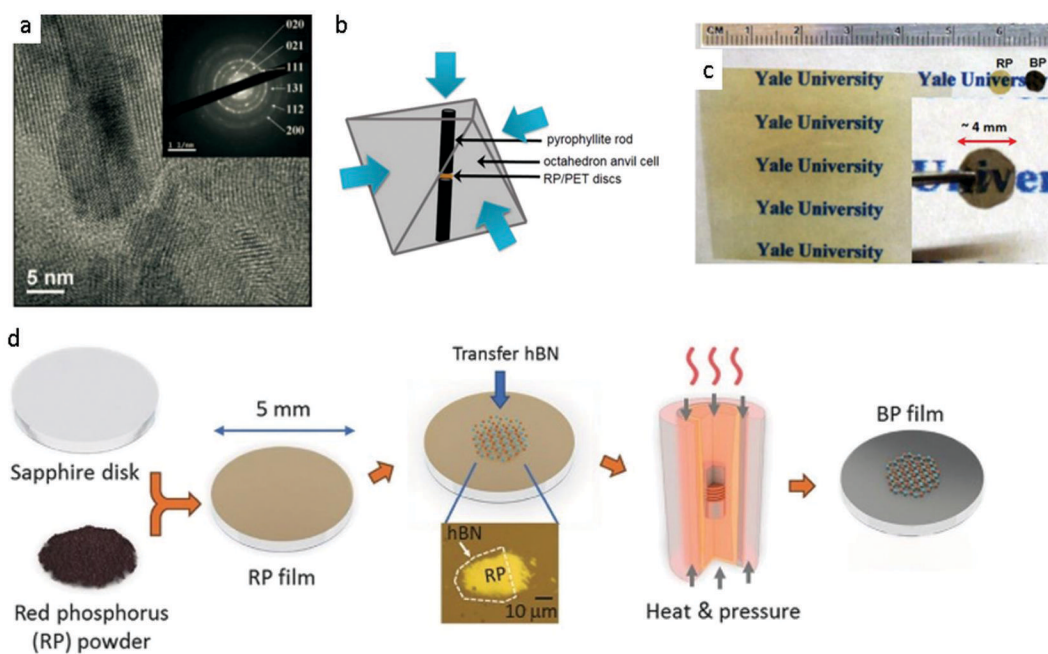


Figure 12. (a) TEM image of the ball-milling synthesized black phosphorus-carbon black nanocomposite as a lithium-ion battery electrode material (6). Reproduced with permission from reference (6). Copyright 2007 John Wiley and Sons. (b) Schematic apparatus for the pressurization synthesis of black phosphorus thin film (68). Republished with permission of IOP Publishing, from Li, X.; Deng, B.; Wang, X.; Chen, S.; Vaisman, M.; Karato, S.-i.; Pan, G.; Lee, M. L.; Cha, J.; Wang, H. Synthesis of thin-film black phosphorus on a flexible substrate. *2D Mater.* 2015, 2 (3), 031002.. (c) Optical photo of the synthesized black phosphorus thin film on a PET substrate (68). Republished with permission of IOP Publishing, from Li, X.; Deng, B.; Wang, X.; Chen, S.; Vaisman, M.; Karato, S.-i.; Pan, G.; Lee, M. L.; Cha, J.; Wang, H. Synthesis of thin-film black phosphorus on a flexible substrate. *2D Mater.* 2015, 2 (3), 031002. (d) Schematic diagram of the synthesis process of the crystalline black phosphorus thin film on a sapphire substrate (69). Reproduced with permission from reference (69). Copyright 2018 John Wiley and Sons.

It is worth to mention that all above-mentioned methods are for the preparation of few-layer black phosphorus flakes, the scale of each flake is usually down to micrometer size, which is not suitable for large-area production. Li et al. first reported a method for synthesis of large-area black phosphorus thin film on polyester (PET), the pressurization synthesis schematic and the optical image of the resulted sample are exhibited in Figure 12 (b) and (c) (68). A red phosphorus thin film was firstly deposited on PET, which is subsequently pressurized in an anvil cell for conversion to black phosphorus film. The schematic and as-prepared sample are shown in Fig. 3. This conversion process is conducted at room temperature with a pressure higher than 8 GPa for complete conversion from red phosphorus to black phosphorus. The size of the as-synthesized continuous film is up to 4 mm. However, the crystalline size of converted black phosphorus was around 10 nm, which limited its electronic property. Afterward, Li et al. from the same group reported the synthesis of highly crystalline black phosphorus thin film on a sapphire substrate using a similar method, as illustrated in Figure 12 (d) (69). With the assistance of high temperature at 700°C, the red phosphorus to black phosphorus conversion and crystallization can be completed at a lower pressure of 1.5 GPa. The scale of as prepared continuous black phosphorus thin film is over 600 μm, besides, large single crystal domain size reaches over 70 μm is also achieved. Liu et al. also developed a similar pressurization

strategy for the preparation of graphene film sandwiched poly-crystalline black phosphorus for sodium-ion battery electrode material research (70). The red phosphorus/graphene sandwich-structure film was first synthesized through the vaporization-condensation method, and then a high-pressure of 8 GPa was introduced to convert part of the red phosphorus to black phosphorus at room temperature.

Other Methods

Solvothermal reaction involving solid-vapor-solid transformation can also be used to synthesize amorphous/poly-crystalline black phosphorus nanomaterials. Zhang et al. reported the synthesis of phosphorus nanosheets, and the synthesis schematic and the TEM image of the product were exhibited in Figure 13 (a) and (b), respectively (71). The red phosphorus and ethanol were heated in a stainless-steel high-pressure reactor at 400°C, and then the nanosheet samples were separated by centrifuge at 10000 rpm. The resultant solution was observed to be black in color, and the nanosheets were characterized as amorphous phosphorus phase with weak crystalline black phosphorus signal.

Recently, a top-down process for the phosphorene nanoribbon synthesis was reported by Watts et al. (72) They presented a method to prepare high-quality, individual phosphorene nanoribbon by ionic scissoring of bulk black phosphorus crystals, and the synthesis schematic was presented in Figure 14 (a). In this study, a stable liquid dispersion of phosphorene nanoribbon can be obtained by the designed top-down process methods. The dimension of the fabricated phosphorene nanoribbons are around 4-50nm in width and up to 75 μm in length with the aspect ratio of up to 1000, as shown in TEM image (Figure 14 (b) with the optical image of the suspension inserted). These nanoribbons are single-crystalline and aligned exclusively in the zigzag crystallographic orientation. The method for preparation can be described as below. First, macroscopic bulk black phosphorus crystals are intercalated with lithium ions via an ammonia-based method at low temperature. Then, the acquired composite is immersed in an aprotic solvent followed by the mechanical agitation to produce a stable liquid suspension of phosphorene nanoribbons. The highly directional and rapid intercalation of lithium ions can break the longer P-P bonds along the zigzag direction, leading to the formation of ribbon-like fragments in lithium-black phosphorus compound. The layers materials are negatively charged by the ion intercalation, and thus the following sonication or stirring can be applied to fully exfoliate individual ribbons when placing the intercalated anionic phosphorene crystals in an appropriate polar solvent.

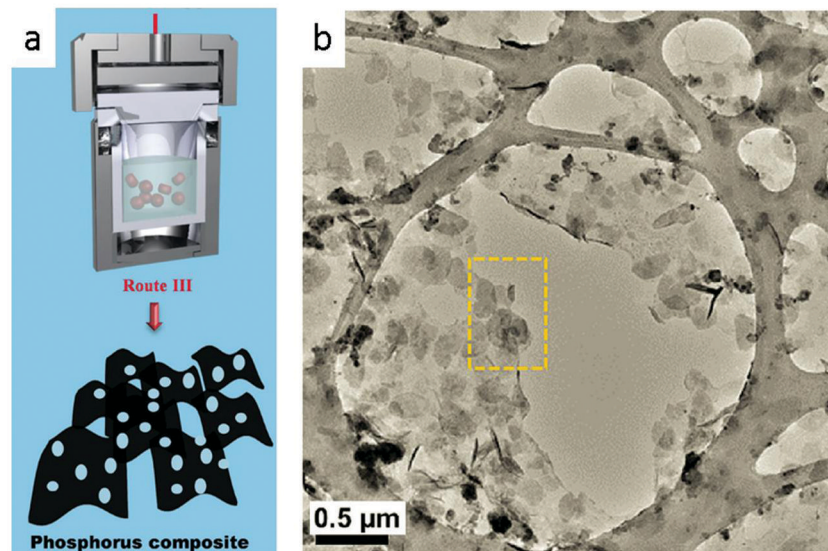


Figure 13. (a) Schematic diagram of the wet-chemical synthesis of phosphorus nanosheets (71). (b) TEM image of the wet-chemically synthesized polycrystalline holey black phosphorus nanosheets (71). Reproduced with permission from reference (71). Copyright 2016 John Wiley and Sons. Copyright 2016 John Wiley and Sons.

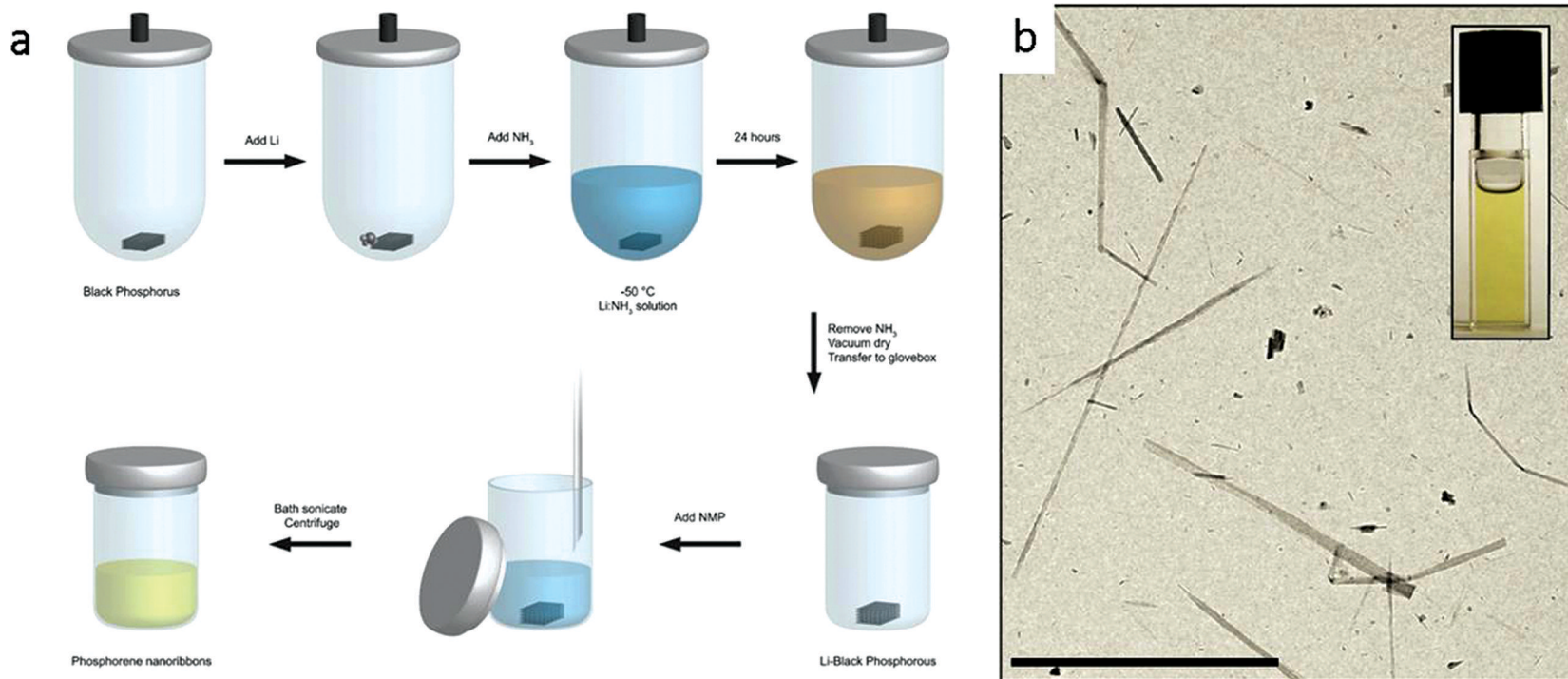


Figure 14. (a) Schematic diagram of the production process of the black phosphorus nanoribbon (72). (b) TEM micrograph of black phosphorus nanoribbon drop-cast from the liquid dispersion shown in the inset, where the scale bar is 10 μm (72). Reprinted by permission from Springer Nature Customer Service Centre GmbH: Springer Nature, Nature, Watts, Mitchell C., Picco, L.; Russell-Pavier, F. S.; Cullen, P. L.; Miller, T. S.; Bartuś, S. P.; Payton, O. D.; Skipper, N. T.; Tileli, V.; Howard, C. A. Production of phosphorene nanoribbons. *Nature* 2019, 568, 216-220, Copyright 2019.

References

1. Ashley, K.; Cordell, D.; Mavinic, D. A brief history of phosphorus: from the philosopher's stone to nutrient recovery and reuse. *Chemosphere* **2011**, *84* (6), 737–746.
2. Liu, W.; Zhi, H.; Yu, X. Recent progress in phosphorus based anode materials for lithium/sodium ion batteries. *Energy Storage Mater.* **2019**, *16*, 290–322.
3. Roth, W.; DeWitt, T.; Smith, A. J. Polymorphism of red phosphorus. *J. Am. Chem. Soc.* **1947**, *69* (11), 2881–2885.
4. Hultgren, R.; Gingrich, N.; Warren, B. The atomic distribution in red and black phosphorus and the crystal structure of black phosphorus. *J. Chem. Phys.* **1935**, *3* (6), 351–355.
5. Wang, F.; Ng, W. K. H.; Jimmy, C. Y.; Zhu, H.; Li, C.; Zhang, L.; Liu, Z.; Li, Q. Red phosphorus: an elemental photocatalyst for hydrogen formation from water. *Appl. Catal., B* **2012**, *111*, 409–414.
6. Park, C. M.; Sohn, H. J. Black phosphorus and its composite for lithium rechargeable batteries. *Adv. Mater.* **2007**, *19* (18), 2465–2468.
7. Qian, J.; Qiao, D.; Ai, X.; Cao, Y.; Yang, H. Reversible 3-Li storage reactions of amorphous phosphorus as high capacity and cycling-stable anodes for Li-ion batteries. *Chem. Commun.* **2012**, *48* (71), 8931–8933.
8. Qian, J.; Wu, X.; Cao, Y.; Ai, X.; Yang, H. High capacity and rate capability of amorphous phosphorus for sodium ion batteries. *Angew. Chem. Int. Ed.* **2013**, *52* (17), 4633–4636.
9. Kim, Y.; Park, Y.; Choi, A.; Choi, N. S.; Kim, J.; Lee, J.; Ryu, J. H.; Oh, S. M.; Lee, K. T. An amorphous red phosphorus/carbon composite as a promising anode material for sodium ion batteries. *Adv. Mater.* **2013**, *25* (22), 3045–3049.
10. Li, W.-J.; Chou, S.-L.; Wang, J.-Z.; Liu, H.-K.; Dou, S.-X. Simply mixed commercial red phosphorus and carbon nanotube composite with exceptionally reversible sodium-ion storage. *Nano Lett.* **2013**, *13* (11), 5480–5484.
11. Song, J.; Yu, Z.; Gordin, M. L.; Hu, S.; Yi, R.; Tang, D.; Walter, T.; Regula, M.; Choi, D.; Li, X. Chemically bonded phosphorus/graphene hybrid as a high performance anode for sodium-ion batteries. *Nano Lett.* **2014**, *14* (11), 6329–6335.
12. Marino, C.; Debenedetti, A.; Fraisse, B.; Favier, F.; Monconduit, L. Activated-phosphorus as new electrode material for Li-ion batteries. *Electrochem. Commun.* **2011**, *13* (4), 346–349.
13. Liu, Y.; Zhang, A.; Shen, C.; Liu, Q.; Cao, X.; Ma, Y.; Chen, L.; Lau, C.; Chen, T.-C.; Wei, F. Red phosphorus nanodots on reduced graphene oxide as a flexible and ultra-fast anode for sodium-ion batteries. *ACS Nano* **2017**, *11* (6), 5530–5537.
14. Liu, Y.; Zhang, A.; Shen, C.; Liu, Q.; Cai, J.; Cao, X.; Zhou, C. Single-step flash-heat synthesis of red phosphorus/graphene flame-retardant composite as flexible anodes for sodium-ion batteries. *Nano Res.* **2018**, *11* (7), 3780–3790.
15. Zhu, Y.; Wen, Y.; Fan, X.; Gao, T.; Han, F.; Luo, C.; Liou, S.-C.; Wang, C. Red phosphorus–single-walled carbon nanotube composite as a superior anode for sodium ion batteries. *ACS Nano* **2015**, *9* (3), 3254–3264.
16. Li, W.; Yang, Z.; Jiang, Y.; Yu, Z.; Gu, L.; Yu, Y. Crystalline red phosphorus incorporated with porous carbon nanofibers as flexible electrode for high performance lithium-ion batteries. *Carbon* **2014**, *78*, 455–462.

17. Li, W.; Yang, Z.; Li, M.; Jiang, Y.; Wei, X.; Zhong, X.; Gu, L.; Yu, Y. Amorphous red phosphorus embedded in highly ordered mesoporous carbon with superior lithium and sodium storage capacity. *Nano Lett.* **2016**, *16* (3), 1546–1553.
18. Li, W.; Hu, S.; Luo, X.; Li, Z.; Sun, X.; Li, M.; Liu, F.; Yu, Y. Confined amorphous red phosphorus in MOF-derived N-doped microporous carbon as a superior anode for sodium-ion battery. *Adv. Mater.* **2017**, *29* (16), 1605820.
19. Ruck, M.; Hoppe, D.; Wahl, B.; Simon, P.; Wang, Y.; Seifert, G. Fibrous red phosphorus. *Angew. Chem. Int. Ed.* **2005**, *44* (46), 7616–7619.
20. Comsup, N.; Panpranot, J.; Praserttham, P. The effect of phosphorous precursor on the CO oxidation activity of P-modified TiO₂ supported Ag catalysts. *Catal. Commun.* **2010**, *11* (15), 1238–1243.
21. Wang, F.; Ng, W. K. H.; Jimmy, C. Y.; Zhu, H.; Li, C.; Zhang, L.; Liu, Z.; Li, Q. Red phosphorus: an elemental photocatalyst for hydrogen formation from water. *Appl. Catal., B* **2012**, *111*, 409–414.
22. Brown, A.; Rundqvist, S. Refinement of the crystal structure of black phosphorus. *Acta Crystallogr.* **1965**, *19* (4), 684–685.
23. Winchester, R. A.; Whitby, M.; Shaffer, M. S. Synthesis of pure phosphorus nanostructures. *Angew. Chem. Int. Ed.* **2009**, *48* (20), 3616–3621.
24. Liu, Y.; Hu, Z.; Jimmy, C. Y. Liquid bismuth initiated growth of phosphorus microbelts with efficient charge polarization for photocatalysis. *Appl. Catal., B* **2019**, *247*, 100–106.
25. Chang, W.-C.; Tseng, K.-W.; Tuan, H.-Y. Solution synthesis of iodine-doped red phosphorus nanoparticles for lithium-ion battery anodes. *Nano Lett.* **2017**, *17* (2), 1240–1247.
26. Liu, S.; Xu, H.; Bian, X.; Feng, J.; Liu, J.; Yang, Y.; Yuan, C.; An, Y.; Fan, R.; Ci, L. Nanoporous red phosphorus on reduced graphene oxide as superior anode for sodium-ion batteries. *ACS Nano* **2018**, *12* (7), 7380–7387.
27. Zhou, J.; Liu, X.; Cai, W.; Zhu, Y.; Liang, J.; Zhang, K.; Lan, Y.; Jiang, Z.; Wang, G.; Qian, Y. Wet-chemical synthesis of hollow red-phosphorus nanospheres with porous shells as anodes for high-performance lithium-ion and sodium-ion batteries. *Adv. Mater.* **2017**, *29* (29), 1700214.
28. Gao, H.; Zhou, T.; Zheng, Y.; Liu, Y.; Chen, J.; Liu, H.; Guo, Z. Integrated Carbon/Red Phosphorus/Graphene Aerogel 3D Architecture via Advanced Vapor-Redistribution for High-Energy Sodium-Ion Batteries. *Adv. Energy Mater.* **2016**, *6* (21), 1601037.
29. Pei, L.; Zhao, Q.; Chen, C.; Liang, J.; Chen, J. Phosphorus Nanoparticles Encapsulated in Graphene Scrolls as a High-Performance Anode for Sodium-Ion Batteries. *ChemElectroChem* **2015**, *2* (11), 1652–1655.
30. Sun, J.; Lee, H.-W.; Pasta, M.; Sun, Y.; Liu, W.; Li, Y.; Lee, H. R.; Liu, N.; Cui, Y. Carbothermic reduction synthesis of red phosphorus-filled 3D carbon material as a high-capacity anode for sodium ion batteries. *Energy Storage Mater.* **2016**, *4*, 130–136.
31. Shulenburg, L.; Baczewski, A. D.; Zhu, Z.; Guan, J.; Tomanek, D. The nature of the interlayer interaction in bulk and few-layer phosphorus. *Nano Lett.* **2015**, *15* (12), 8170–8175.
32. Bridgman, P. Two New Modifications of phosphorus. *J. Am. Chem. Soc.* **1914**, *36* (7), 1344–1363.
33. Bridgman, P. Two new phenomena at very high pressure. *Phys. Rev.* **1934**, *45* (11), 844.

34. Bridgman, P. Effects of high shearing stress combined with high hydrostatic pressure. *Phys. Rev.* **1935**, *48* (10), 825.
35. Brown, A.; Rundqvist, S. Refinement of the crystal structure of black phosphorus. *Acta Crystallogr.* **1965**, *19* (4), 684–685.
36. Endo, S.; Akahama, Y.; Terada, S.-i.; Narita, S.-i. Growth of large single crystals of black phosphorus under high pressure. *Jpn. J. Appl. Phys.* **1982**, *21* (8A), L482.
37. Lange, S.; Schmidt, P.; Nilges, T. Au₃SnP₇@ black phosphorus: an easy access to black phosphorus. *Inorg. Chem.* **2007**, *46* (10), 4028–4035.
38. Nilges, T.; Kersting, M.; Pfeifer, T. A fast low-pressure transport route to large black phosphorus single crystals. *J. Solid State Chem.* **2008**, *181* (8), 1707–1711.
39. Rissi, E. N.; Soignard, E.; McKiernan, K. A.; Benmore, C. J.; Yarger, J. L. Pressure-induced crystallization of amorphous red phosphorus. *Solid State Commun.* **2012**, *152* (5), 390–394.
40. Li, L.; Yu, Y.; Ye, G. J.; Ge, Q.; Ou, X.; Wu, H.; Feng, D.; Chen, X. H.; Zhang, Y. Black phosphorus field-effect transistors. *Nat. Nanotechnol.* **2014**, *9* (5), 372.
41. Liu, H.; Neal, A. T.; Zhu, Z.; Luo, Z.; Xu, X.; Tománek, D.; Ye, P. D. Phosphorene: an unexplored 2D semiconductor with a high hole mobility. *ACS Nano* **2014**, *8* (4), 4033–4041.
42. Castellanos-Gomez, A.; Vicarelli, L.; Prada, E.; Island, J. O.; Narasimha-Acharya, K.; Blanter, S. I.; Groenendijk, D. J.; Buscema, M.; Steele, G. A.; Alvarez, J. Isolation and characterization of few-layer black phosphorus. *2D Mater.* **2014**, *1* (2), 025001.
43. Lu, W.; Nan, H.; Hong, J.; Chen, Y.; Zhu, C.; Liang, Z.; Ma, X.; Ni, Z.; Jin, C.; Zhang, Z. Plasma-assisted fabrication of monolayer phosphorene and its Raman characterization. *Nano Res.* **2014**, *7* (6), 853–859.
44. Brent, J. R.; Savjani, N.; Lewis, E. A.; Haigh, S. J.; Lewis, D. J.; O'Brien, P. Production of few-layer phosphorene by liquid exfoliation of black phosphorus. *Chem. Commun.* **2014**, *50* (87), 13338–13341.
45. Yasaei, P.; Kumar, B.; Foroozan, T.; Wang, C.; Asadi, M.; Tuschel, D.; Indacochea, J. E.; Klie, R. F.; Salehi-Khojin, A. High-quality black phosphorus atomic layers by liquid-phase exfoliation. *Adv. Mater.* **2015**, *27* (11), 1887–1892.
46. Sun, J.; Lee, H.-W.; Pasta, M.; Yuan, H.; Zheng, G.; Sun, Y.; Li, Y.; Cui, Y. A Phosphorene-Graphene Hybrid Material as a High-Capacity Anode for Sodium-Ion Batteries. *Nat. Nanotech.* **2015**, *10*, 980–985.
47. Kang, J.; Wood, J. D.; Wells, S. A.; Lee, J.-H.; Liu, X.; Chen, K.-S.; Hersam, M. C. Solvent exfoliation of electronic-grade, two-dimensional black phosphorus. *ACS Nano* **2015**, *9* (4), 3596–3604.
48. Hanlon, D.; Backes, C.; Doherty, E.; Cucinotta, C. S.; Berner, N. C.; Boland, C.; Lee, K.; Harvey, A.; Lynch, P.; Gholamvand, Z. Liquid exfoliation of solvent-stabilized few-layer black phosphorus for applications beyond electronics. *Nat. Commun.* **2015**, *6*, 8563.
49. Chen, L.; Zhou, G.; Liu, Z.; Ma, X.; Chen, J.; Zhang, Z.; Ma, X.; Li, F.; Cheng, H. M.; Ren, W. Scalable clean exfoliation of high-quality few-layer black phosphorus for a flexible lithium ion battery. *Adv. Mater.* **2016**, *28* (3), 510–517.
50. Sun, Z.; Xie, H.; Tang, S.; Yu, X. F.; Guo, Z.; Shao, J.; Zhang, H.; Huang, H.; Wang, H.; Chu, P. K. Ultrasmall black phosphorus quantum dots: synthesis and use as photothermal agents. *Angew. Chem. Int. Ed.* **2015**, *54* (39), 11526–11530.

51. Zhang, X.; Xie, H.; Liu, Z.; Tan, C.; Luo, Z.; Li, H.; Lin, J.; Sun, L.; Chen, W.; Xu, Z. Black phosphorus quantum dots. *Angew. Chem. Int. Ed.* **2015**, *54* (12), 3653–3657.
52. Erande, M. B.; Suryawanshi, S. R.; More, M. A.; Late, D. J. Electrochemically exfoliated black phosphorus nanosheets—prospective field emitters. *Eur. J. Inorg. Chem.* **2015**, *2015* (19), 3102–3107.
53. Erande, M. B.; Pawar, M. S.; Late, D. J. Humidity sensing and photodetection behavior of electrochemically exfoliated atomically thin-layered black phosphorus nanosheets. *ACS Appl. Mater. Interfaces* **2016**, *8* (18), 11548–11556.
54. Huang, Z.; Hou, H.; Zhang, Y.; Wang, C.; Qiu, X.; Ji, X. Layer-Tunable Phosphorene Modulated by the Cation Insertion Rate as a Sodium-Storage Anode. *Adv. Mater.* **2017**, *29* (34), 1702372.
55. Li, J.; Chen, C.; Liu, S.; Lu, J.; Goh, W. P.; Fang, H.; Qiu, Z.; Tian, B.; Chen, Z.; Yao, C. Ultrafast Electrochemical Expansion of Black Phosphorus toward High-Yield Synthesis of Few-Layer Phosphorene. *Chem. Mater.* **2018**, *30* (8), 2742–2749.
56. Wang, C.; He, Q.; Halim, U.; Liu, Y.; Zhu, E.; Lin, Z.; Xiao, H.; Duan, X.; Feng, Z.; Cheng, R.; Weiss, N.; Ye, G.; Huang, Y. C.; Wu, H.; Cheng, H. C.; Shakir, I.; Liao, L.; Chen, X.; Goddard, W.; Huang, Y.; Duan, X. Monolayer atomic crystal molecular superlattices. *Nature* **2018**, *555*, 231–236.
57. Lin, Z.; Liu, Y.; Halim, U.; Ding, M.; Liu, Y.; Wang, Y.; Jia, C.; Chen, P.; Duan, X.; Wang, C. Solution-processable 2D semiconductors for high-performance large-area electronics. *Nature* **2018**, *562* (7726), 254.
58. Bat-Erdene, M.; Batmunkh, M.; Shearer, C. J.; Tawfik, S. A.; Ford, M. J.; Yu, L.; Sibley, A. J.; Slattery, A. D.; Quinton, J. S.; Gibson, C. T. Efficient and Fast Synthesis of Few-Layer Black Phosphorus via Microwave-Assisted Liquid-Phase Exfoliation. *Small Methods* **2017**, *1* (12), 1700260.
59. Smith, J. B.; Hagaman, D.; Ji, H.-F. Growth of 2D black phosphorus film from chemical vapor deposition. *Nanotechnology* **2016**, *27* (21), 215602.
60. Yang, Z.; Hao, J.; Yuan, S.; Lin, S.; Yau, H. M.; Dai, J.; Lau, S. P. Field-effect transistors based on amorphous black phosphorus ultrathin films by pulsed laser deposition. *Adv. Mater.* **2015**, *27* (25), 3748–3754.
61. Xu, H.; Han, X.; Li, Z.; Liu, W.; Li, X.; Wu, J.; Guo, Z.; Liu, H. Epitaxial Growth of Few-Layer Black Phosphorene Quantum Dots on Si Substrates. *Adv. Mater. Interfaces* **2018**, *5* (21), 1801048.
62. Jiang, Q.; Xu, L.; Chen, N.; Zhang, H.; Dai, L.; Wang, S. Facile synthesis of black phosphorus: an efficient electrocatalyst for the oxygen evolving reaction. *Angew. Chem. Int. Ed.* **2016**, *55* (44), 13849–13853.
63. Zhu, Z.; Tománek, D. Semiconducting layered blue phosphorus: a computational study. *Phys. Rev. Lett.* **2014**, *112* (17), 176802.
64. Zhang, J. L.; Zhao, S.; Han, C.; Wang, Z.; Zhong, S.; Sun, S.; Guo, R.; Zhou, X.; Gu, C. D.; Yuan, K. D. Epitaxial growth of single layer blue phosphorus: a new phase of two-dimensional phosphorus. *Nano Lett.* **2016**, *16* (8), 4903–4908.

65. Xu, J.-P.; Zhang, J.-Q.; Tian, H.; Xu, H.; Ho, W.; Xie, M. One-dimensional phosphorus chain and two-dimensional blue phosphorene grown on Au (111) by molecular-beam epitaxy. *Phys. Rev. Mater.* **2017**, *1* (6), 061002.
66. Gu, C.; Zhao, S.; Zhang, J. L.; Sun, S.; Yuan, K.; Hu, Z.; Han, C.; Ma, Z.; Wang, L.; Huo, F. Growth of quasi-free-standing single-layer blue phosphorus on tellurium monolayer functionalized Au (111). *ACS Nano* **2017**, *11* (5), 4943–4949.
67. Aldave, S. H.; Yogeesh, M. N.; Zhu, W.; Kim, J.; Sonde, S. S.; Nayak, A. P.; Akinwande, D. Characterization and sonochemical synthesis of black phosphorus from red phosphorus. *2D Mater.* **2016**, *3* (1), 014007.
68. Li, X.; Deng, B.; Wang, X.; Chen, S.; Vaisman, M.; Karato, S.-i.; Pan, G.; Lee, M. L.; Cha, J.; Wang, H. Synthesis of thin-film black phosphorus on a flexible substrate. *2D Mater.* **2015**, *2* (3), 031002.
69. Li, C.; Wu, Y.; Deng, B.; Xie, Y.; Guo, Q.; Yuan, S.; Chen, X.; Bhuiyan, M.; Wu, Z.; Watanabe, K. Synthesis of crystalline black phosphorus thin film on sapphire. *Adv. Mater.* **2018**, *30* (6), 1703748.
70. Liu, Y.; Liu, Q.; Zhang, A.; Cai, J.; Cao, X.; Li, Z.; Asimow, P. D.; Zhou, C. Room-Temperature Pressure Synthesis of Layered Black Phosphorus–Graphene Composite for Sodium-Ion Battery Anodes. *ACS Nano* **2018**, *12* (8), 8323–8329.
71. Zhang, Y.; Rui, X.; Tang, Y.; Liu, Y.; Wei, J.; Chen, S.; Leow, W. R.; Li, W.; Liu, Y.; Deng, J. Wet-Chemical Processing of Phosphorus Composite Nanosheets for High-Rate and High-Capacity Lithium-Ion Batteries. *Adv. Energy Mater.* **2016**, *6* (10), 1502409.
72. Watts, M. C.; Picco, L.; Russell-Pavier, F. S.; Cullen, P. L.; Miller, T. S.; Bartuś, S. P.; Payton, O. D.; Skipper, N. T.; Tileli, V.; Howard, C. A. Production of phosphorene nanoribbons. *Nature* **2019**, *568*, 216–220.